INTERNATIONAL JOURNAL FOR NUMERICAL METHODS IN FLUIDS
Int. J. Numer. Meth. Fluids 2004; **44**:1163–1184 (DOI: 10.1002/fld.694)

Adaptive strategy of the supersonic turbulent flow over a backward-facing step

Shih-Ying Yang*,†

Department of Aeronautical Engineering, National Huwei Institute of Technology, Huwei, Yunlin 632, Taiwan, ROC

SUMMARY

An adaptive strategy incorporating mesh remeshing and refining is developed to study the supersonic turbulent flow over a backward-facing step on a mixed quadrilateral–triangular mesh. In the Cartesian co-ordinate system, the unsteady Favre-averaged Navier–Stokes equations with a low-Reynolds-number k–ε turbulence model are solved using a locally implicit scheme with an anisotropic dissipation model. In the present adaptive strategy, two error indicators for both mesh remeshing and refining, respectively, are presented. The remeshing error indicator incorporates unified magnitude of substantial derivative of pressure and that of vorticity magnitude, whereas the refining error indicator incorporates unified magnitude of substantial derivative of pressure and that of weighted vorticity magnitude. To assess the present approach, the transonic turbulent flow around an NACA 0012 airfoil is performed. Based on the comparison with the experimental data, the accuracy of the present approach is confirmed. According to the high-resolutional result on the adaptive mesh, the structure of backstep corner vortex, expansion wave and oblique shock wave is distinctly captured. Copyright © 2004 John Wiley & Sons, Ltd.

KEY WORDS: adaptive; remeshing; refining; locally implicit; backward-facing step

1. INTRODUCTION

Several applications including scramjet, missile, rocket and spacecraft may directly benefit from further understanding the supersonic flow over a backward-facing step. Research of flow separation and reattachment at supersonic speeds is commonly conducted in backward-facing step configurations. Such a flowfield can be described as a supersonic flow that turns beyond the step corner through an expansion fan, and turns back to a direction approximately parallel to the inflow by an oblique reattachment shock wave. McDonald [1] and Rom [2] applied the momentum integral method to obtain the base pressure, where flow conditions in

*Correspondence to: S.-Y. Yang, Department of Aeronautical Engineering, National Huwei Institute of Technology, Huwei, Yunlin 632, Taiwan, Republic of China.
†E-mail: anneyang@sunws.nhit.edu.tw

Contract/grant sponsor: National Science Council of the Republic of China; contract/grant number: NSC 91-2212-E-150-026

Received 30 July 2003
Accepted 10 December 2003

the reattachment zone were explicitly described. Recently, non-intrusive optical methods such as the laser Doppler velocimetry (LDV) [3–5] and planar laser-induced fluorescence (PLIF) [6] have been applied to measure the flow properties directly. A number of CFD researchers solved Euler [7, 8] and Navier–Stokes [5, 9–13] equations to investigate the supersonic flows over a backward-facing step. Loth *et al.* [7] utilized the finite element method-flux corrected transport algorithm and adaptive unstructured gridding to solve the unsteady Euler equations. Yang [8] presented an error indicator in which the unified magnitude of pressure gradient and unified magnitude of gradient of vorticity magnitude were incorporated to study the supersonic inviscid flow over a backward-facing step. The mesh refinement with a two-level refinement procedure was employed. Arai *et al.* [5] applied the total variation diminishing (TVD) finite-difference scheme, in which eddy viscosity was determined using Baldwin–Lomax turbulence model. Kuruvila and Anderson [9] solved the Navier–Stokes equations by means of MacCormack scheme with a fourth-order numerical dissipation term. They concluded that the numerical dissipation had virtually no effect on the results for an adiabatic wall case. On patched mesh systems, Lombard *et al.* [10] used the implicit upwind scheme, which was based on a characteristic eigenvector decomposition of the spatially averaged flux difference Jacobian matrix. Yang *et al.* [11] employed a flux-vector splitting lower–upper symmetric successive overrelaxation scheme, and deduced that reduction of the base pressure and recirculation zone could cause difficulties in ignition and flameholding in Scramjet combustors. Tucker and Shyy [12] introduced the FDNS code [14], in which k–ε turbulence model was corrected to treat compressible flows. Halupovich *et al.* [13] utilized the PHOENICS code and k–ε turbulence model to investigate the supersonic backstep flow. The PHOENICS code was found to be adequate for supersonic flow simulation with $M \leqslant 3.5$. However, convergence was not obtained at hypersonic turbulent flow conditions.

As mentioned by Sheng *et al.* [15], the biggest advantage of the unstructured grid approach over the structured grid approach is that the process of grid generation for complex geometries is greatly simplified. Also mentioned by Mavriplis [16], unstructured grid techniques offered the potential for greatly reducing the grid generation time associated with complex geometries. Furthermore, unstructured mesh approaches enabled the use of adaptive meshing techniques, which held great promise for increasing solution accuracy at minimal additional computational cost. Recently, considerable effort has been made to develop solution-adaptive techniques [17–23] for solving the Euler/Navier–Stokes equations on unstructured meshes. The mesh-enrichment and mesh-coarsening procedures [17] were implemented within an unstructured grid upwind-type Euler code, and the absolute value of the substantial derivative of density was used as an enrichment indicator. By using the two-step Runge–Kutta Galerkin finite element method and a local remeshing technique [18], a shock propagation within a channel was investigated. From the time-varying meshes, directionally stretched elements were demonstrated. Webster *et al.* [19] developed an adaptive finite element methodology, in which the finite quadtree mesh generator, interpolation-based error indicator and edge-based mesh enrichment procedure were employed. A grid refinement technique [20], which was based on a combination of surface mesh subdivision and local remeshing of the volume grid, was developed and successfully applied to several three-dimensional flow test cases. Walsh and Zingg [21] presented a solution-dependent retriangulation algorithm which locally restructured the grid to recover an anisotropic grid following adaptation. For the blade–vortex interaction problems on unstructured meshes, a solution-adaptive dynamic mesh scheme [22] was used by adding and deleting mesh points at every adaptation step to take account of not only spatial

but also of temporal variations of the flowfield. In the author's previous study [23], a refining error indicator was used in which unified magnitudes of dynamic grid speed, substantial derivative of pressure, and substantial derivative of vorticity magnitude were incorporated to study inviscid transonic flows over vibrating blades with interblade phase angles.

In the present calculation of the supersonic turbulent flow over a backward-facing step, the remeshing error indicator proposed by Hwang and Wu [18] is modified to incorporate the pressure and vorticity magnitude as the remeshing key variable to treat the new node spacing, whereas the refining error indicator proposed in the author's previous study [23] is modified by weighting the vorticity magnitude to account for the viscous effect. The locally implicit scheme was originally developed by Reddy and Jacock [24] on structured quadrilaterals. This scheme is locally implicit, but globally explicit. Hwang and Liu [25] developed the locally implicit scheme and anisotropic dissipation model on triangular mesh. In the author's previous study [23], the locally implicit scheme and anisotropic dissipation model were developed on the mixed quadrilateral–triangular mesh for inviscid flow calculations. In this study, the locally implicit scheme and anisotropic dissipation model are extended for turbulent flow calculations. As far as the turbulence model is concerned, the low-Reynolds-number k–ε turbulence model proposed by Abe *et al.* [26] is adopted. This model was modified from the low-Reynolds-number k–ε turbulence model of Nagano and Tagawa [27]. It had been shown that the separation and reattaching flows downstream of a backward-facing step were simulated quite successfully.

There are three objectives in the present study: (1) to develop an adaptive strategy for the supersonic turbulent flow over a backward-facing step; (2) to develop a locally implicit scheme with anisotropic dissipation model on a quadrilateral–triangular mesh for turbulent flow calculations; and (3) to investigate the supersonic turbulent flow over a backward-facing step.

2. GOVERNING EQUATIONS

The two-dimensional, unsteady Favre-averaged Navier–Stokes equations with a two-equation low-Reynolds-number k–ε turbulence model in non-dimensionalized form can be written as

$$\frac{\partial U}{\partial t}+\frac{\partial E}{\partial x}+\frac{\partial G}{\partial y}=\frac{1}{Re}\left[\frac{\partial E_v}{\partial x}+\frac{\partial G_v}{\partial y}\right]+S \tag{1}$$

where

$$U=\begin{bmatrix}\rho\\ \rho u\\ \rho v\\ e\\ \rho k\\ \rho\varepsilon\end{bmatrix},\quad E=\begin{bmatrix}\rho u\\ \rho u^2+p^*\\ \rho uv\\ (e+p^*)u\\ \rho uk\\ \rho u\varepsilon\end{bmatrix},\quad G=\begin{bmatrix}\rho v\\ \rho uv\\ \rho v^2+p^*\\ (e+p^*)v\\ \rho vk\\ \rho v\varepsilon\end{bmatrix}$$

$$E_v = \begin{bmatrix} 0 \\ \tau_{xx} \\ \tau_{xy} \\ E_{v4} \\ (\mu_\ell + \dfrac{\mu_t}{\sigma_k})k_x \\ (\mu_\ell + \dfrac{\mu_t}{\sigma_\varepsilon})\varepsilon_x \end{bmatrix}, \quad G_v = \begin{bmatrix} 0 \\ \tau_{xy} \\ \tau_{yy} \\ G_{v4} \\ \left(\mu_\ell + \dfrac{\mu_t}{\sigma_k}\right) k_y \\ \left(\mu_\ell + \dfrac{\mu_t}{\sigma_\varepsilon}\right) \varepsilon_y \end{bmatrix}, \quad S = \begin{bmatrix} 0 \\ 0 \\ 0 \\ 0 \\ S_k \\ S_\varepsilon \end{bmatrix}$$

$$\tau_{xx} = 2\mu u_x + \lambda(u_x + v_y)$$

$$\tau_{yy} = 2\mu v_y + \lambda(u_x + v_y)$$

$$\tau_{xy} = \mu(u_y + v_x)$$

$$E_{v4} = u\tau_{xx} + v\tau_{xy} + \frac{1}{\gamma - 1}\left(\frac{\mu_\ell}{Pr_\ell} + \frac{\mu_t}{Pr_t}\right) T_x$$

$$G_{v4} = u\tau_{xy} + v\tau_{yy} + \frac{1}{\gamma - 1}\left(\frac{\mu_\ell}{Pr_\ell} + \frac{\mu_t}{Pr_t}\right) T_y$$

$$Pr_\ell = 0.72, \quad Pr_t = 0.9, \ \gamma = 1.4$$

$$\mu = \mu_\ell + \mu_t$$

$$\lambda = -\tfrac{2}{3}\,\mu$$

$$P^* = P + \tfrac{2}{3}\,\rho k$$

$$S_k = P_k - \rho\varepsilon$$

$$S_\varepsilon = \frac{\varepsilon}{k}\,(C_1 f_1 P_k - C_2 f_2 \rho\varepsilon)$$

$$P_k = \frac{1}{Re}\,\mu_t \left[2(u_x^2 + v_y^2) + (v_x + u_y)^2 - \frac{2}{3}(u_x + v_y)^2\right] - \frac{2}{3}(u_x + v_y)\rho k$$

$$\mu_t = Re\,\rho C_\mu f_\mu k^2/\varepsilon$$

$$f_\mu = \left[1 - \exp\left(-\frac{y^*}{14}\right)\right]^2 \left\{1 + \frac{5}{R_t^{3/4}}\,\exp\left[-\left(\frac{R_t}{200}\right)^2\right]\right\}$$

$$y^* = \frac{u_\varepsilon y}{\upsilon_\ell}\,Re^{3/4}, \quad u_\varepsilon = (\upsilon_\ell \varepsilon)^{1/4}$$

$$R_t = \frac{k^2}{\upsilon_\ell \varepsilon} Re$$

$$f_1 = 1$$

$$f_2 = \left[1 - \exp\left(-\frac{y^*}{3.1}\right)\right]^2 \left\{1 - 0.3 \exp\left[-\left(\frac{R_t}{6.5}\right)^2\right]\right\}$$

Model constants

$$C_\mu = 0.09, \quad \sigma_k = \sigma_\varepsilon = 1.4, \quad C_1 = 1.5, \quad C_2 = 1.9$$

Variables ρ, u, v and e represent the gas density, velocity component in x, y directions and the total energy per unit volume, respectively. Pressure P is given by the equation of state, and γ is the ratio of specific heat.

$$P = (\gamma - 1)\left[e - \frac{\rho}{2}(u^2 + v^2) - \rho k\right] \tag{2}$$

In the present calculation, the low-Reynolds-number k–ε turbulence model proposed by Abe *et al*. [26] is adopted. This model was modified from the low-Reynolds-number model of Nagano and Tagawa [27]. The principal improvement of this turbulence model [26] is the usage of Kolmogorov velocity scale $u_\varepsilon = (\upsilon_\ell \varepsilon)^{1/4}$ instead of the friction velocity $u_\tau (u_\tau = \sqrt{\tau_\omega/\rho}$, $\tau_\omega =$ wall shear stress) to account for the near-wall and low-Reynolds-number effect. The Kolmogorov velocity scale u_ε becomes zero neither at the separating nor at the reattaching points in contrast to the friction velocity u_τ. It had been shown that the separation and reattaching flows downstream of a backward-facing step were simulated quite successfully. By integrating Equation (1) over space and using Gauss's theorem, the following expression is obtained:

$$\frac{\partial}{\partial t}\int_\Omega U \, \mathrm{d}A + \int_{\partial\Omega} (\mathbf{F}_\mathrm{c} - \mathbf{F}_v) \cdot \mathrm{d}\mathbf{l} = \int_\Omega S \, \mathrm{d}A \tag{3}$$

where

$$\mathbf{F}_\mathrm{c} = E\mathbf{i} + G\mathbf{j}$$

$$\mathbf{F}_\mathrm{v} = \frac{1}{R_e}(E_\mathrm{v}\mathbf{i} + G_\mathrm{v}\mathbf{j})$$

$\mathrm{d}\mathbf{l} = \hat{n}\,\mathrm{d}\ell$ and $\hat{n}$ is the unit normal vector in the outward direction. $\mathbf{F}_\mathrm{c}$ and $\mathbf{F}_\mathrm{v}$ represent the convective and viscous flux vectors, respectively. Ω is the domain of interest and $\partial\Omega$ is the boundary of domain. A fully implicit finite-volume discretization scheme is applied to Equation (3) over the entire flowfield. Flow variables at cell faces are obtained from the averages of flow variables at the cell centres. These values and artificial dissipation terms are introduced for line integral and numerical stability. Then, for each quadrilateral or triangular cell i, Equation (3) becomes

$$A_i\left(\frac{U^{n+1} - U^n}{\Delta t}\right)_i + Q_i^\mathrm{c}(U^{n+1}) - D_i(U^{n+1}) = Q_i^\mathrm{v}(U^n) + S_i^n A_i \tag{4}$$

where

$$Q_i^c(U) = \sum_{k=1}^{N_i} (\mathbf{F}_c \cdot \mathrm{d}\mathbf{l})_{ik}$$

$$Q_i^v(U) = \sum_{k=1}^{N_i} (\mathbf{F}_v \cdot \mathrm{d}\mathbf{l})_{ik}$$

$$N_i = \begin{cases} 3 \text{ for triangular cell } i, \\ 4 \text{ for quadrilateral cell } i \end{cases}$$

A_i, n, and D_i represent the cell area, marching time step and artificial dissipation operator, respectively.

On the structured grid system, Jameson *et al.* [28] developed an effective form for D_i. The isotropic value for scaling the dissipation has been extended to unstructured triangular meshes by Mavriplis [29]. On the static triangular mesh, Hwang and Liu [25] developed the anisotropic dissipation model. In the author's previous study [23], the anisotropic dissipation model was developed on the mixed quadrilateral–triangular mesh for inviscid flow calculations. In this article, the anisotropic dissipation is extended on a quadrilateral–triangular mesh for turbulent flow calculations and described as follows:

$$D_i(U) = \sum_{k=1}^{N_i} d_{ik} \tag{5}$$

where

$$d_{ik} = \varepsilon_{ik}^{(2)}(U_k - U_i) - \varepsilon_{ik}^{(4)}(\nabla^2 U_k - \nabla^2 U_i)$$

$$\varepsilon_{ik}^{(2)} = k^{(2)} \psi_{ik} \bar{\nu}_{ik}$$

$$\varepsilon_{ik}^{(4)} = k^{(4)} \psi_{ik} \max[0, (1 - 32\bar{\nu}_{ik})]$$

$$\psi_{ik} = (|\mathbf{V} \cdot \mathrm{d}\mathbf{l}| + a|\mathrm{d}\mathbf{l}|)_{ik}$$

$$\nu_{ik} = \frac{|\nabla^2 p_i|}{\sum_{k=1}^{N_i} (p_i + p_k)}$$

$$\bar{\nu}_{ik} = \begin{cases} \max(\nu_i, \nu_k, \nu_{k1}, \nu_{k2}, \nu_{k3}), & N_k = 3 \\ \max(\nu_i, \nu_k, \nu_{k1}, \nu_{k2}, \nu_{k3}, \nu_{k4}), & N_k = 4 \end{cases}$$

$$\nabla^2 U_i = \sum_{k=1}^{N_i} U_k - N_i U_i$$

The subscripts $k1, k2$ and $k3$ represent the indices of three adjacent cells which surround the triangular cell k, whereas the subscripts $k1, k2, k3$ and $k4$ represent the indices of four adjacent cells which surround the quadrilateral cell k. $\nabla^2 U_i$ is expressed as an undivided Laplacian

operator. ψ_{ik} is the spectral radius of Jacobian matrix $(\partial \mathbf{F}_c/\partial U \cdot d\mathbf{l})$ on the interface between cell i and cell k. Two constants $k^{(2)}$ and $k^{(4)}$ are taken as 1.0 and $\frac{1}{32}$, respectively.

To improve the convergence speed, a local time stepping technique is imposed as follows:

$$\left(\frac{A}{\Delta t}\right)_i = \frac{\sum_{k=1}^{N_i} \psi_{ik}}{CFL} \tag{6}$$

where CFL is the Courant–Friedrichs–Lewy number. In order to perform the Taylor series expansion for temporal difference, the term $D_i(U^n) - Q_i^c(U^n)$ is added to both the right- and left-hand sides of Equation (4) in advance. Then, Taylor series expansion for temporal difference is implemented on both $Q_i^c(U^{n+1}) - Q_i^c(U^n)$ and $D_i(U^{n+1}) - D_i(U^n)$, respectively. After the linearization, Equation (4) can be constructed in the delta form as follows:

$$L_i(\Delta U) = Re\, s_i^n = -Q_i^c(U^n) + D_i(U^n) + Q_i^v(U^n) + S_i^n A_i \tag{7}$$

where

$$L_i(\Delta U) = CI\,\Delta U_i + \sum_{L=1}^{N_i} CK_L \Delta U_L + \sum_{k=1}^{N_i} \varepsilon_{ik}^{(4)} \sum_{j=1}^{N_k} \Delta U_j$$

$$CI = \frac{1}{2}\left(\sum_{k=1}^{N_i} M_{ik}\right) + \left(\frac{\sum_{k=1}^{N_i} \psi_{ik}}{\mathrm{CFL}} + \sum_{k=1}^{N_i} \varepsilon_{ik}^{(2)} + N_i \sum_{k=1}^{N_i} \varepsilon_{ik}^{(4)}\right) I$$

$$CK_L = \frac{1}{2} M_{iL} - \left(\varepsilon_{iL}^{(2)} + N_L \varepsilon_{iL}^{(4)} + \sum_{k=1}^{N_i} \varepsilon_{ik}^{(4)}\right) I$$

$$I = \mathrm{Diag}[1, 1, 1, 1, 1, 1]$$

$$M_{ik} = \left(\frac{\partial \mathbf{F}_c}{\partial U} \cdot d\mathbf{l}\right)_{ik}$$

To solve Equation (7), a locally implicit scheme [24, 30] is implemented. This scheme is locally implicit, but globally explicit and is unconditionally stable under local linearized analysis [30]. It does not require the assembly of any global matrices and does not need any matrix system solvers. The locally implicit scheme is originally developed by Reddy and Jacock [24] on structured quadrilaterals. Hwang and Liu [25] developed the locally implicit scheme and anisotropic dissipation model on a triangular mesh. In the author's previous study [23], the locally implicit scheme and anisotropic dissipation model were developed on the mixed quadrilateral–triangular mesh for inviscid flow calculations. In this study, the locally implicit scheme and anisotropic dissipation model are extended on a quadrilateral–triangular mesh for turbulent flow calculations.

For each cell i, the equation for iterative corrections is written as

$$C\,dU_i = \mathrm{Res}_i^n - L_i(\Delta U) \tag{8}$$

$$\Delta U_i^{(m+1)} = \Delta U_i^{(m)} + W_{\mathrm{in}}\,dU_i, \quad m = 1, 2 \tag{9}$$

where C is a diagonal matrix defined as a modification to the coefficient CI

$$C = \left[\frac{\sum_{k=1}^{N_i} \psi_{ik}}{\mathrm{CFL}} \left(1.0 + \frac{\mathrm{CFL}}{2} \right) + 0.5 \left(\sum_{k=1}^{N_i} \varepsilon_{ik}^{(2)} + N_i \sum_{k=1}^{N_i} \varepsilon_{ik}^{(4)} \right) \right] I \tag{10}$$

ΔU shown on the right-hand side of Equation (8) takes the latest available values from Equation (9). The inner iteration for $\Delta U^{(m+1)}$ can be computed rapidly since the $\mathrm{d}U$ corrections are explicit scalar equations. Starting at the first element and sweeping to the latest element, two symmetric inner iterations are performed at each time step. At the end of a time step, the outer relaxation is introduced.

$$U_i^{n+1} = U_i^n + W_{\mathrm{out}} \Delta U_i \tag{11}$$

The coefficients W_{in} and W_{out} in Equations (9) and (11) are inner and outer relaxation parameters of order 1.2.

3. ADAPTIVE-MESH ALGORITHM

An adaptive strategy incorporating mesh remeshing and refining is developed in this paper to study the supersonic turbulent flow over a backward-facing step on a quadrilateral–triangular mesh. It is well known that error indicators play an important role in the solution-adaptive procedures. In the present adaptive strategy, two error indicators for both mesh remeshing and refining, respectively, are presented. The remeshing error indicator incorporates unified magnitude of substantial derivative of pressure and that of vorticity magnitude, whereas the refining error indicator incorporates unified magnitude of substantial derivative of pressure and that of weighted vorticity magnitude. The initial mesh is remeshed first according to the initial solution and the corresponding remeshing error indicator is adopted to treat the new node spacing. Then, the remeshed mesh is refined and the corresponding refining error indicator is applied.

As far as the mesh remeshing is concerned, Hwang and Wu [18] developed a simple and direct error indicator for remeshing instead of using second derivatives as the error indicators. As mentioned by Hwang and Wu [18], node spacing for remeshing must be smaller in regions of large change in properties, and was evaluated by the following expression.

$$\delta_d^2 |\nabla \phi|_d = \mathrm{CT} \tag{12}$$

where ϕ is the selected key variable, δ_d the spacing at node d, and $|\nabla \phi|_d$ the absolute value of the gradient of ϕ at node d.

The constant CT in Equation (12) was determined by the product of the square of a specified minimum node spacing and the absolute value of the maximum solution gradient over the whole mesh, i.e.

$$\mathrm{CT} = \delta_{d,\min}^2 |\nabla \phi|_{\max} \tag{13}$$

In the present paper, the constant CT in Equation (12) is determined by the product of the square of a specified average node spacing and the average absolute value of the solution gradients over the whole mesh, i.e.

$$\mathrm{CT} = \delta_{d,\mathrm{avg}}^2 |\nabla \phi|_{\mathrm{avg}} \tag{14}$$

The objective of substituting Equation (14) for Equation (13) is to avoid that the use of a maximum absolute gradient may give results which are strongly dependent on the behaviour of the single point whose solution gradient is the largest. Furthermore, when the flow properties become smooth over the entire computational domain, the number of remeshing cells will increase significantly, which is due to the fact that all the values of node spacing are almost equal to the specified minimum value. This drawback can also be overcome by substituting Equation (14) for Equation (13). In order to control the largest and smallest sizes of the remeshing cells, al1 the values of node spacing computed by Equations (12) and (14) must be limited to the specified maximum and minimum values.

As for the selection of the key variable ϕ, density is chosen by Hwang and Wu [18]. In the present calculations, the steady solution is achieved on the initial non-adaptive mesh in advance. According to the initial grid and steady solution, the new node spacing of mesh remeshing is accomplished by calculating Equations (12) and (14), and pressure is employed as the key variable. It is found that the new mesh is capable of capturing the oblique shock wave and expansion wave. However, it is unable to capture the structure of the backstep corner vortex. To capture the structure of backstep corner vortex, the vorticity magnitude ($w = |\nabla \times \mathbf{v}|$) is implemented as the key variable ϕ to reperform the mesh remeshing. According to the adaptive mesh using w as the key variable ϕ in Equations (12) and (14), the structure of backstep corner vortex is captured clearly. However, it cannot capture the oblique shock wave and expansion wave behaviour.

In order to capture the structure of backstep corner vortex, Prandtl–Meyer expansion wave and oblique shock wave simultaneously, Equation (12) is modified and written as follows:

$$\delta_d^2 \left(\frac{|\mathrm{D}p/\mathrm{D}t|_d}{|\mathrm{D}p/\mathrm{D}t|_{\max}} + \beta \frac{|\mathrm{D}w/\mathrm{D}t|_d}{|\mathrm{D}w/\mathrm{D}t|_{\max}} \right) = \mathrm{CT}_2 \tag{15}$$

where

$$\mathrm{CT}_2 = \delta_{d,\mathrm{avg}}^2 \left(\frac{|\mathrm{D}p/\mathrm{D}t|_d}{|\mathrm{D}p/\mathrm{D}t|_{\max}} + \beta \frac{|\mathrm{D}w/\mathrm{D}t|_d}{|\mathrm{D}w/\mathrm{D}t|_{\max}} \right)_{\mathrm{avg}} \tag{16}$$

$|\mathrm{D}p/\mathrm{D}t|_{\max}$ and $|\mathrm{D}w/\mathrm{D}t|_{\max}$ are the maximum values of $|\mathrm{D}p/\mathrm{D}t|$ and $|\mathrm{D}w/\mathrm{D}t|$ among the computational cells, respectively. w is the vorticity magnitude ($w = |\nabla \times \mathbf{v}|$) and β represents the weighted coefficient chosen as 1.0. Since the order of magnitude of $|\mathrm{D}w/\mathrm{D}t|$ outnumbers that of $|\mathrm{D}p/\mathrm{D}t|$, it is essential to adjust both at the same order. Hence, $|\mathrm{D}p/\mathrm{D}t|$ and $|\mathrm{D}w/\mathrm{D}t|$ are divided by $|\mathrm{D}p/\mathrm{D}t|_{\max}$ and $|\mathrm{D}w/\mathrm{D}t|_{\max}$, respectively. According to the initial grid and steady solution, the new node spacing of remeshing is accomplished by calculating Equations (15) and (16). After achieving the new node spacing, the technique of stretching direction and ratio of stretching developed by Hwang and Wu [18] is also applied. Then, the mixed quadrilateral–triangular mesh is obtained from a combination process, which couples two triangles into a new quadrilateral when the common side of the two triangles is the longest one of these two triangles.

As for the initial quadrilateral–triangular mesh of supersonic turbulent backstep flow calculation, two thin layers of quadrilaterals are distributed along both upper and lower walls to simulate boundary layer effects, and quadrilaterals are also distributed in the upstream area ahead of backward-facing step to allow quick stretching in the upstream direction. Besides these quadrilaterals, triangles are generated elsewhere. During remeshing, the triangular mesh

is remeshed first according to the present remeshing error indicator and steady solution on the initial mesh. Then, quadrilaterals are remeshed according to the boundaries connected to the remeshed triangles. The present quadrilateral–triangular mesh is treated as a single unstructured mesh, and interfaces between quadrilaterals and triangles are removed. Therefore, the irregularities at the interfaces between the regions with quadrilateral and triangular elements do not affect the solutions.

As far as the mesh refining is concerned, the refining error indicator and refinement technique are presented. In the author's previous inviscid study [23], an error indicator, which incorporated the unified magnitudes of dynamic grid speed, substantial derivative of pressure and substantial derivative of vorticity magnitude was proposed and formulated as

$$\mathrm{EI} = \frac{|\mathrm{D}P/\mathrm{D}t|}{|\mathrm{D}p/\mathrm{D}t|_{\max}} + \beta_1 \frac{|\mathrm{D}w/\mathrm{D}t|}{|\mathrm{D}w/\mathrm{D}t|_{\max}} + \beta_2 \frac{|\mathbf{V}_g|}{|\mathbf{V}_g|_{\max}} \tag{17}$$

where $|\mathrm{D}p/\mathrm{D}t|$, $|\mathrm{D}w/\mathrm{D}t$ and $|\mathbf{V}_g|$ are the absolute values of the substantial derivative of pressure, substantial derivative of vorticity magnitude and velocity vector of dynamic grid, respectively. $|\mathrm{D}p/\mathrm{D}t|_{\max}$, $|\mathrm{D}w/\mathrm{D}t|_{\max}$ and $|\mathbf{V}_g|_{\max}$ are the maximum values of $|\mathrm{D}p/\mathrm{D}t|$, $|\mathrm{D}w/\mathrm{D}t|$ and $|\mathbf{V}_g|$ among all the computational cells, respectively.

In the present turbulent study, the error indicator in Equation (17) is further improved to account for the viscous effect, and the dynamic grid speed effect is removed. The present error indicator is formulated as

$$\begin{aligned} \mathrm{EI} &= \frac{|\mathrm{D}P/\mathrm{D}t|}{|\mathrm{D}p/\mathrm{D}t|_{\max}} + \beta_3 \frac{|\beta^*(\mathrm{D}w/\mathrm{D}t)|}{|\beta^*(\mathrm{D}w/\mathrm{D}t)|_{\max}} \\ \beta^* &= 1 - \mathrm{e}^{-100(Y_{\mathrm{wall}}/H)^2} \end{aligned} \tag{18}$$

where $|\mathrm{D}p/\mathrm{D}t|$ and $|\beta^*(\mathrm{D}w/\mathrm{D}t)|$ are the absolute values of the substantial derivative of pressure, and substantial derivative of weighted vorticity magnitude. Y_{wall} is the minimum distance between the computing cell and the walls, and H is the step height. $|\mathrm{D}p/\mathrm{D}t|_{\max}$ and $|\beta^*(DW/\mathrm{D}t)|_{\max}$ are the maximum values of $|\mathrm{D}p/\mathrm{D}t|$ and $|\beta^*(\mathrm{D}w/\mathrm{D}t)|$ among all the computational cells, respectively. Since the order of magnitude of $|\beta^*(\mathrm{D}w/\mathrm{D}t)|$ outnumbers those of $|\mathrm{D}p/\mathrm{D}t|$, it is essential to adjust both at the same order. Hence, $|\mathrm{D}p/\mathrm{D}t|$ and $|\beta^*(\mathrm{D}w/\mathrm{D}t)|$ are divided by $|\mathrm{D}p/\mathrm{D}t|_{\max}$ and $|\beta^*(\mathrm{D}w/\mathrm{D}t)|_{\max}$, respectively. β^* represents the weighted function and β_3 is the corresponding weighted coefficient. For the calculation of the supersonic turbulent flow over a backward-facing step, β_3 is set to be 1.0. The purpose of imposing β^* in Equation (18) is to counteract the effect that the value of $|\mathrm{D}w/\mathrm{D}t|$ increases abruptly as it approaches the boundary layer, especially in the viscous sublayer. The value of β^* in Equation (18) will decrease abruptly as it approaches the boundary layer, especially in the viscous sublayer.

As for the refinement technique, the value of EI of each unrefined cell is firstly calculated. The product of a specified constant C_1 and the average value of EI over the initial grid is selected as the threshold value. If the value of EI of each unrefined cell is larger than the threshold value $C_1 * \mathrm{EI}_{\mathrm{ave}}$, the new node will be placed at the midpoint of each edge of quadrilateral/triangular cell or the centre of the quadrilateral cell [31]. Normally, the value of C_1 ranges from 0.4 to 0.8. In the present calculation, C_1 is chosen as 0.6. Since Webster *et al.* [19] mentioned that the mesh coarsening accounted for the majority of CPU cost during adaptation, the mesh coarsening procedure is not processed in this article.

4. BOUNDARY CONDITIONS

In the present calculations, no-slip and adiabatic wall conditions are imposed at the body or wall surface. Pressure is obtained by the following condition:

$$(x_\xi^2 + y_\xi^2)P_\eta - (x_\xi x_\eta + y_\xi y_\eta)P_\xi = 0 \tag{19}$$

where η and ξ represent the body-fitted co-ordinate lines. $u = v = k = 0$ and $\varepsilon = 2\upsilon_\ell(\partial\sqrt{k}/\partial\eta)^2$. Density is obtained from the equation of state. As for the far field of transonic turbulent flow around an NACA 0012 airfoil, one-dimensional characteristic analysis based on Riemann invariants is used to determine the values of flow variables on the outer boundary of the computational domain. Considering the supersonic turbulent flow over a backward-facing step, the freestream conditions are specified at inlet and space extrapolation is applied on the exit plane.

5. RESULTS AND DISCUSSION

The present numerical approach is evaluated by performing the transonic turbulent flow around an NACA 0012 airfoil. To further demonstrate the versatility of the present adaptive strategy, the supersonic turbulent flow over a backward-facing step is investigated.

5.1. Transonic turbulent flow around an NACA 0012 airfoil

To evaluate the present solution approach, transonic turbulent flow ($M_\infty = 0.756$, $Re = 4.01 \times 10^6$) around an NACA 0012 airfoil with zero angle of attack is investigated. The computational domain is taken to be $21\mathrm{C} \times 20\mathrm{C}$, where C is the chord length. The quadrilateral–triangular mesh system (see Figure 1) contains 7666 cells and 5819 nodes, and there are 110 points that lie on the airfoil surface. The minimum distance between the cells and the airfoil surface is equal to 1.16×10^{-4} chord. Pressure coefficient distributions on the airfoil surface are depicted in Figure 2. As shown in Figure 2, the calculated pressure coefficient distribution compares well with the experimental data [32]. It is apparent that the present approach is accurate in the turbulent flow calculation.

5.2. Supersonic turbulent flow over a backward–facing step

The supersonic turbulent flow over a backward-facing step is investigated using the present solution algorithm. Geometric configuration and flowfield conditions are the same as those in the experiment [6]. Inlet Mach number, freestream temperature, freestream pressure, freestream velocity and Reynolds number are set to 2.0, 167 K, 34.8 kPa, 520 m/s and 103 300, respectively. The averaged stagnation temperature and stagnation pressure measured in the experiment [6] were 310 K and 273 kPa, respectively. The step height in the experiment was equal to 3.18 mm, whereas the width downstream of the backward-facing step was equal to 20.12 mm. A schematic of this flowfield is shown in Figure 3, in which points Q and A are singular points mathematically. The Mach 2 inlet flow expands through the centred Prandtl–Meyer expansion wave. A recirculation zone, which is essentially the backstep corner vortex, is formed behind the step and below the upper wall. Then the flow is turned back parallel to the upper wall and compressed through an oblique shock wave.

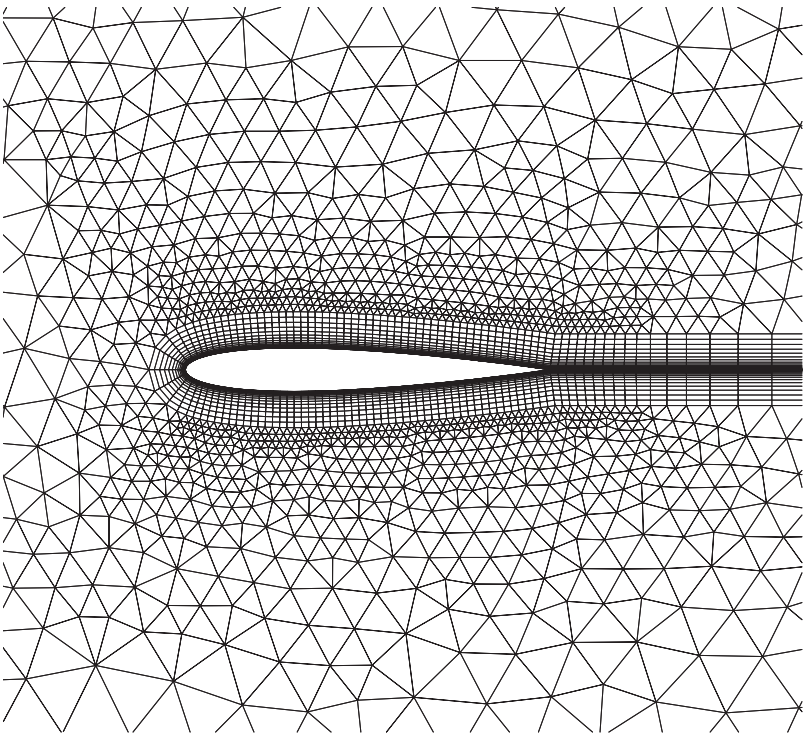

Figure 1. Mesh for transonic turbulent flow around an NACA 0012 airfoil.

The initial mesh shown in Figure 4 incorporates the quadrilaterals and triangles, where the triangles are generated by the global remeshing algorithm [18]. Inside the initial mesh (Figure 4a), the computational domain in front of the step is extended 40 times of step height. As for the initial quadrilateral-triangular mesh (Figures 4(a) and (b)), two thin layers of quadrilaterals are distributed along both upper and lower walls to simulate boundary layer effects, and quadrilaterals are also distributed in the upstream area ahead of the backward-facing step to allow quick stretching in the upstream direction. Besides these quadrilaterals, triangles are generated elsewhere. The initial quadrilateral–triangular mesh is treated as a single unstructured mesh, and interfaces between quadrilaterals and triangles are removed. After obtaining the steady solution on initial mesh, the pressure contour and vorticity contour are depicted in Figures 5 and 6. As shown in Figure 5, pressure remains identical in front of the expansion wave. Pressure drops rapidly across the expansion wave, which is due to flow acceleration. When the flow passes through the oblique shock wave, pressure recovers quickly. As for the backstep corner vortex, there is no evident pressure variation. Considering the vorticity contour (see Figure 6), it is indicated that vorticity gradient only appears in the recirculation zone and boundary layers. To assess the accuracy of the present calculation, the present pressure contour (see Figure 5) is compared to that obtained in the experiment [6] (see Figure 7) and by the PHOENICS code [13] (see Figure 8). Based on the comparison, it is indicated that the present result can accurately capture the structure of Prandtl–Meyer

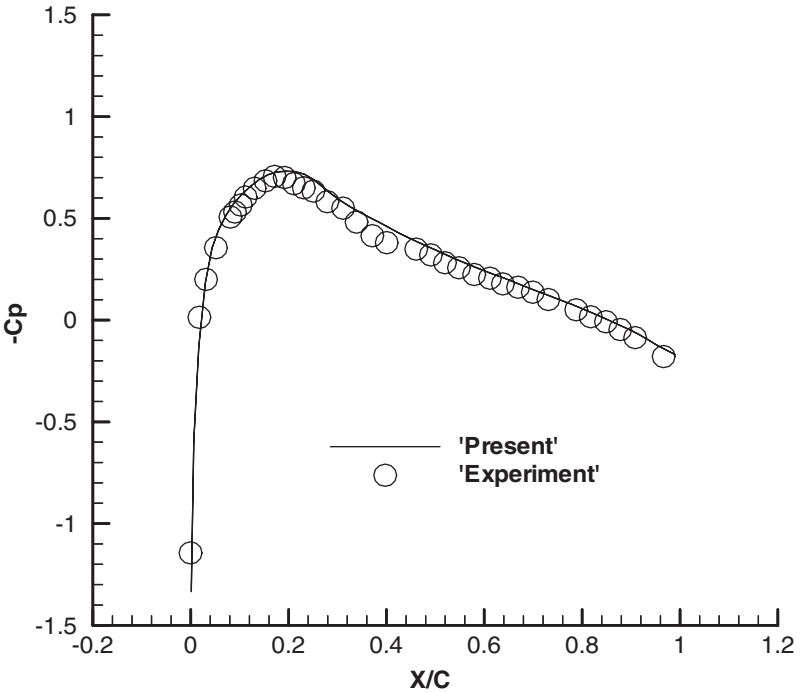

Figure 2. Pressure coefficient distributions for transonic turbulent flow around an NACA 0012 airfoil.

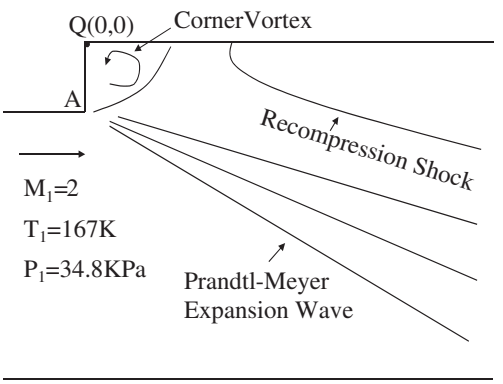

Figure 3. Flowfield schematic of supersonic turbulent flow over a backward-facing step.

expansion wave and oblique shock wave. However, the flowfield resolution on initial mesh is not satisfactory, especially for the expansion wave close to point A and the structure of oblique shock wave.

To promote the flowfield resolution, the error indicator in Equations (12) and (14) is carried out to obtain the new node spacing and pressure is employed as the selected key variable ϕ.

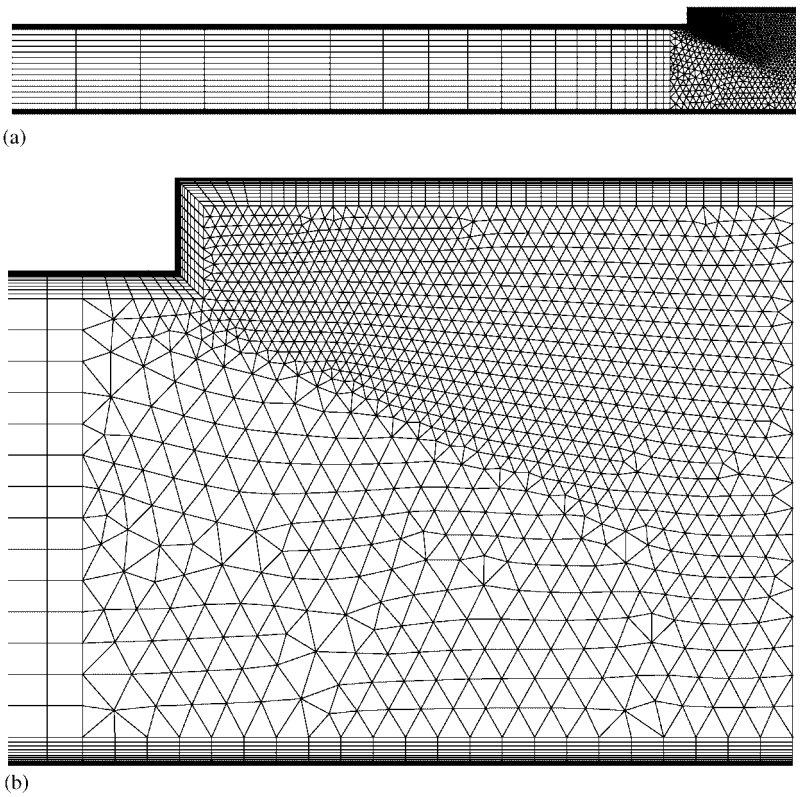

Figure 4. (a) Global view and (b) local view of the initial mesh of supersonic turbulent flow over a backward-facing step (4686 cells).

The maximum and minimum values of node spacing are set to be 0.4 and 0.04, respectively. During remeshing, the technique of directional grid adaptation [18] with stretching ratio 1.1 is applied to the triangles first. Then, quadrilaterals are remeshed according to the boundaries connected to the remeshed triangles. The final quadrilateral–triangular mesh plotted in Figure 9 is obtained from a combination process which couples two triangles into a new quadrilateral when the common side of the two triangles is the longest one of these two triangles. During the combination process, only data with respect to the cells are changed while nodal data remain the same. Therefore, both the computational time and storage can be saved. As shown in Figure 9, the capability of capturing the structure of expansion wave and oblique shock wave is confirmed. However, it is unable to remesh the backstep corner vortex. To capture the structure of backstep corner vortex, the error indicator in Equations (12) and (14) is carried out to obtain the new node spacing whereas vorticity magnitude ($w = |\nabla \times \mathbf{v}|$) is employed as the selected key variable ϕ. The maximum and minimum values of node spacing are set to be 0.4 and 0.04, respectively. The corresponding quadrilateral–triangular mesh is plotted in Figure 10. As demonstrated in Figure 10, the structure of backstep corner vortex is captured precisely. However, it is unable to remesh the structure of expansion wave and oblique shock wave.

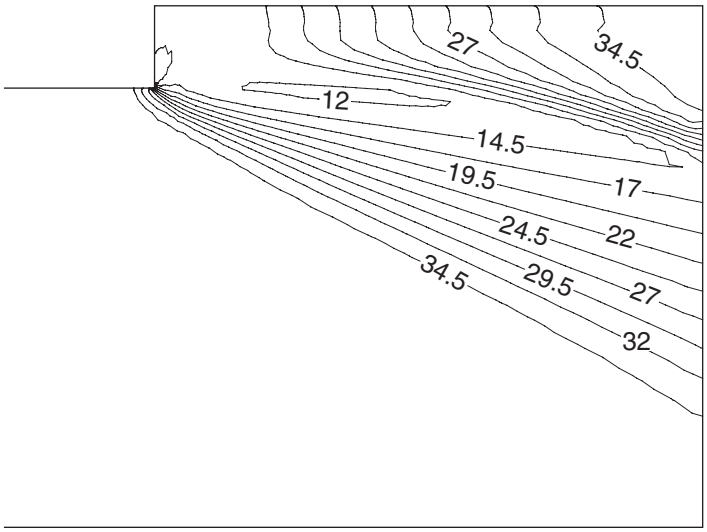

Figure 5. Pressure contour obtained on the initial mesh in Figure 4.

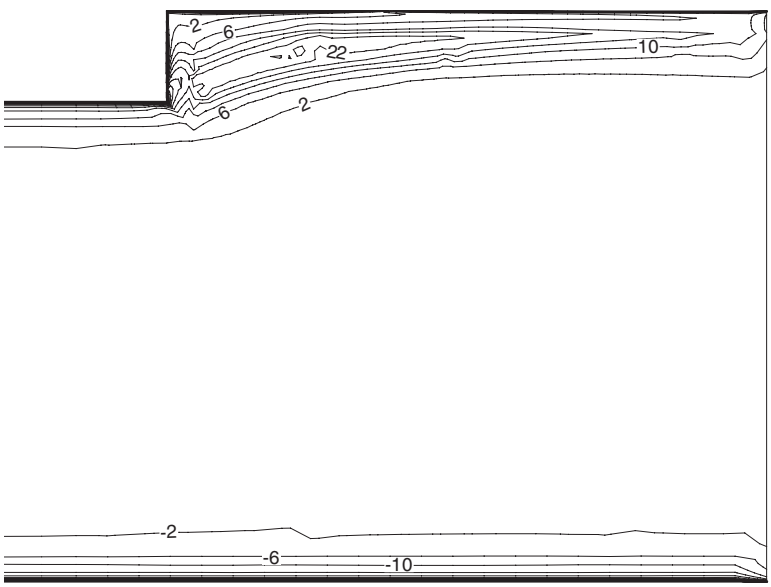

Figure 6. Vorticity contour obtained on the initial mesh in Figure 4.

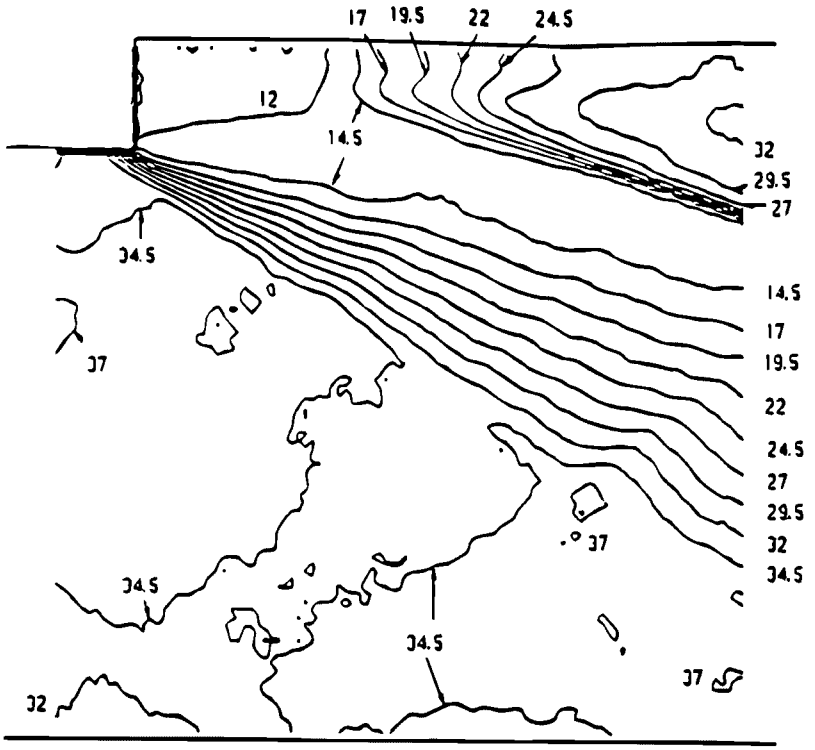

Figure 7. Pressure contour obtained in the experiment [6].

To incorporate the advantages and avoid the disadvantages of the preceding meshes (Figures 9 and 10), the remeshing error indicator is developed in the present paper. Hence, the error indicator in Equations (15) and (16) is used to obtain the new node spacing, and the maximum and minimum values of node spacing are set to be 0.4 and 0.04, respectively. The corresponding remeshed mesh is depicted in Figure 11. In order to promote the flowfield resolution, the refining error indicator in Equation (18) is carried out to refine the mesh on Figure 11. The corresponding refined mesh is plotted in Figure 12. During remeshing, the technique of directional grid adaptation [18] with stretching ratio 1.1 is applied to the triangles first. Then, quadrilaterals are remeshed according to the boundaries connected to the remeshed triangles. The quadrilateral–triangular mesh plotted in Figure 11 is obtained from a combination process which couples two triangles into a new quadrilateral when the common side of the two triangles is the longest one of these two triangles. During the combination process, only data with respect to the cells are changed while nodal data remain the same. Therefore, both the computational time and storage can be saved. During refining, it is noted that the value of $|\mathrm{D}w/\mathrm{D}t|$ increases abruptly as it approaches the boundary layer, especially in the viscous sublayer. Hence, a weighted function β^* in Equation (18) is imposed to counteract the above situation. As demonstrated in the adaptive mesh in Figure 12, the structure of backstep corner vortex, expansion wave and oblique shock wave is clearly indicated. After

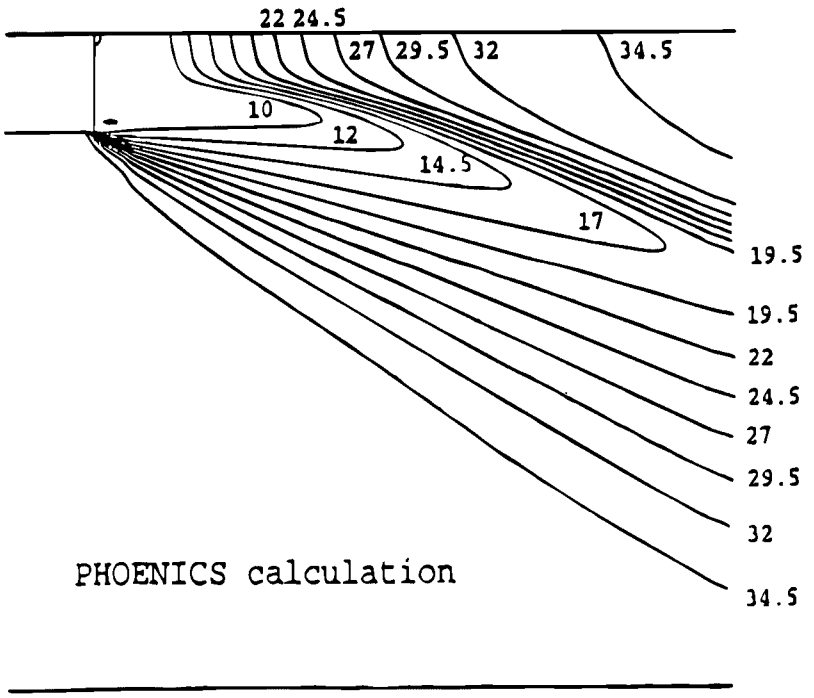

Figure 8. Pressure contour computed by the PHOENICS code [13].

achieving the steady solution on the adaptive mesh in Figure 12, the pressure contour and vorticity contour are plotted in Figures 13 and 14. Comparing the pressure contours (see Figures 5 and 13), the high-resolutional result is demonstrated on the adaptive mesh, especially for the oblique shock wave and expansion wave close to point A. To evaluate the accuracy of the present calculation on adaptive mesh, the present pressure contour (Figure 13) is compared to that obtained in the experiment [6] (Figure 7) and by the PHOENICS code [13] (Figure 8). As demonstrated in Figures 8 and 13, the numerical result obtained by the present adaptive strategy (Figure 13) compares well with that obtained by the PHOENICS code (Figure 8). As far as the experimental data are concerned, the discrepancy is found for pressure contours near the downstream of the upper wall. Besides the aforementioned discrepancy, both the numerical results obtained by the present adaptive strategy (Figure 13) and by the PHOENICS code (Figure 8) match well with the experimental data (Figure 7). Furthermore, the accuracy of the adaptive solution is confirmed. From the vorticity contours (see Figures 6 and 14), it is found that high-resolutional structure of backstep corner vortex is distinctly indicated on the adaptive mesh (Figure 14). For the above calculations, the Fortran 77 adopted as the programming language and computations are performed on the Dec 500ae workstation. The non-adaptive calculation on the initial mesh in Figure 4 takes 2237 s on the Dec 500ae workstation, whereas the adaptive calculation on the adaptive mesh in Figure 12 takes 7945 s on the same workstation.

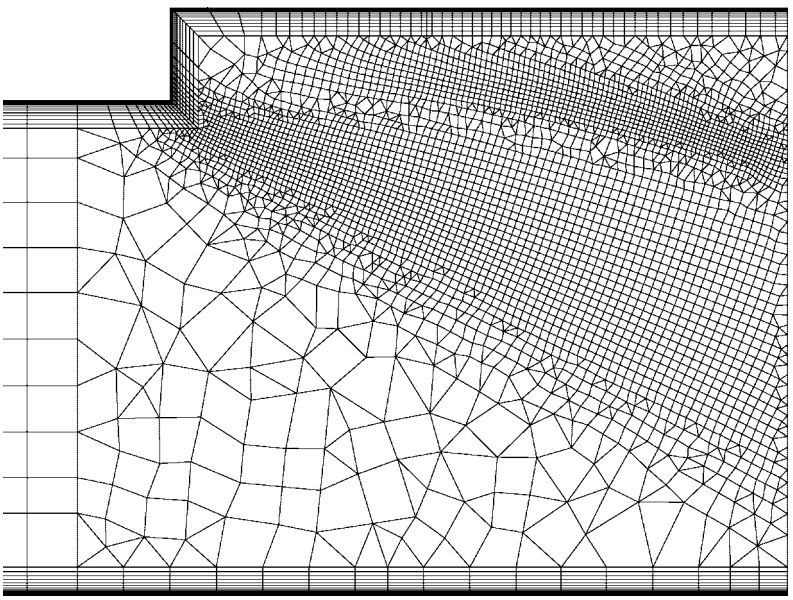

Figure 9. Adaptive mesh obtained using Equation (12) as the error indicator and pressure as the key variable (6441 cells).

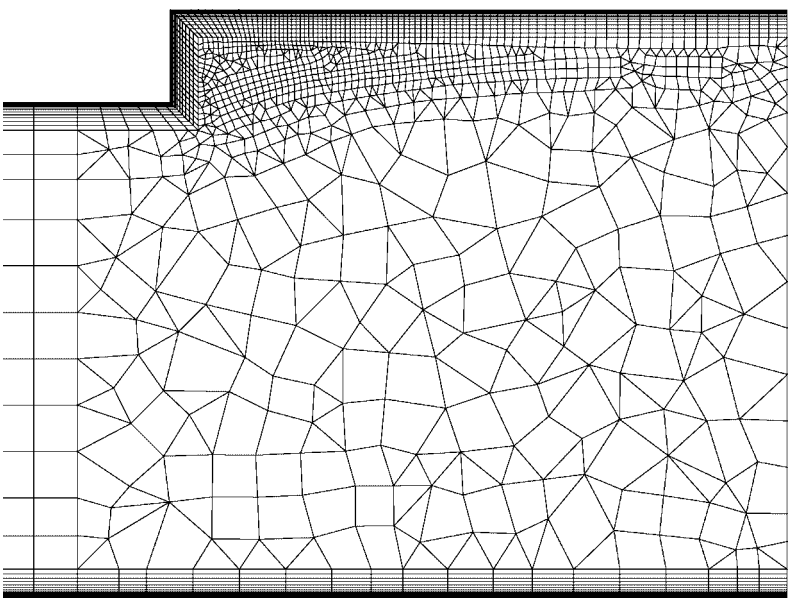

Figure 10. Adaptive mesh obtained using Equation (12) as the error indicator and vorticity magnitudeas the key variable (4420 cells).

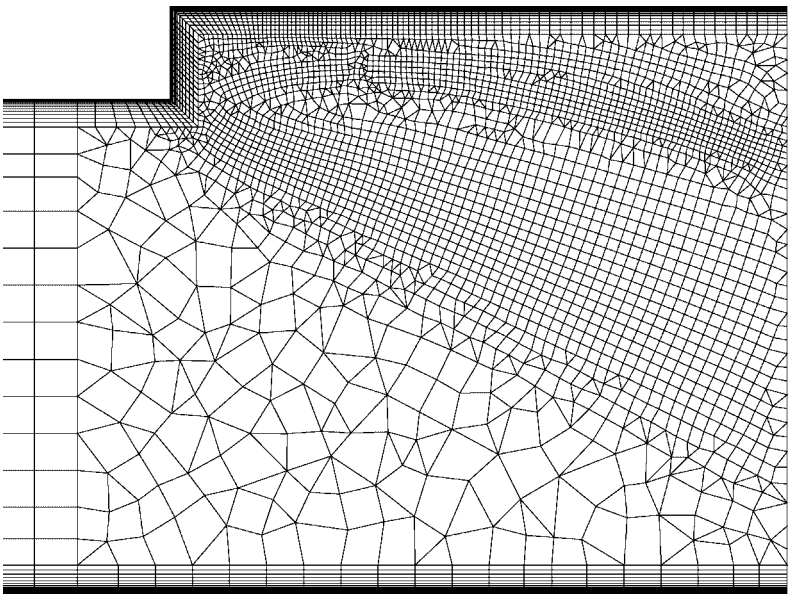

Figure 11. Adaptive mesh obtained using the present remeshing error indicator in Equation (15) (6274 cells).

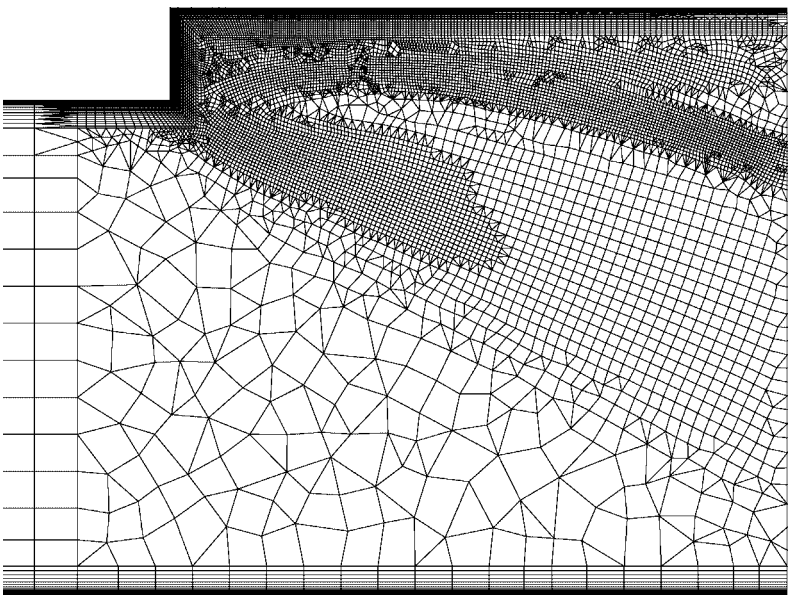

Figure 12. Adaptive mesh obtained using the present adaptive strategy (12 634 cells).

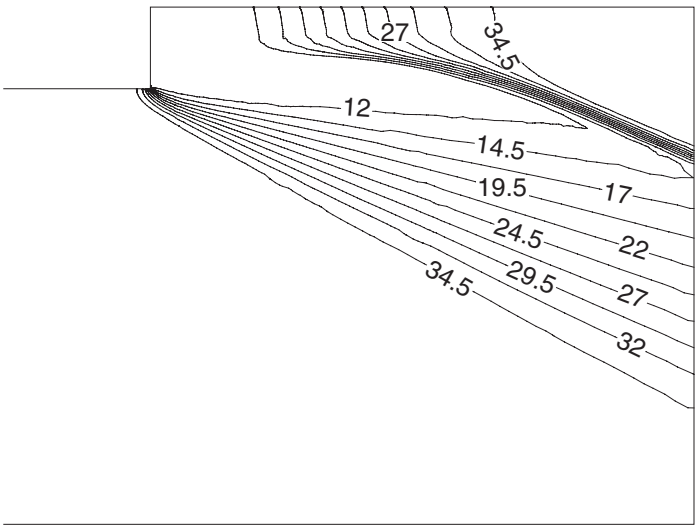

Figure 13. Pressure contour obtained on the adaptive mesh in Figure 12.

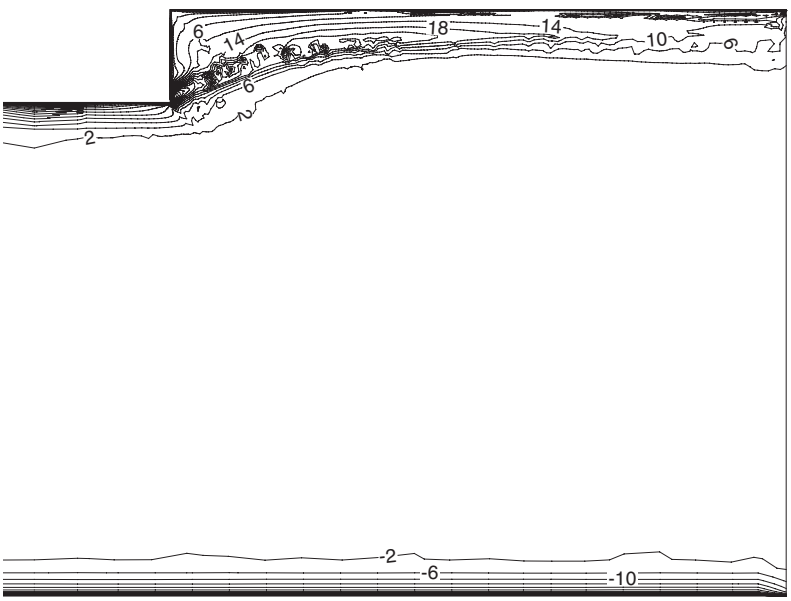

Figure 14. Vorticity contour obtained on the adaptive mesh in Figure 13.

6. CONCLUSIONS

The main contribution of this paper is to develop an adaptive strategy incorporating mesh remeshing as well as refining and a locally implicit scheme with anisotropic dissipation model

on a quadrilateral–triangular mesh to study the supersonic turbulent flow over a backward-facing step. The remeshing error indicator incorporates the unified magnitude of substantial derivative of pressure and that of vorticity magnitude to treat the new node spacing. The refining error indicator incorporates the unified magnitude of substantial derivative of pressure and that of weighted vorticity magnitude. A weighted function is added to the term of vorticity magnitude which substantially counteracts the abrupt increasing vorticity magnitude as it approaches the boundary layer, especially in the viscous sublayer. After performing the transonic turbulent flow around an NACA 0012 airfoil, the accuracy of the present solution algorithm is confirmed by comparing the present result with experimental data. According to the adaptive mesh obtained using the present adaptive strategy, the structure of backstep corner vortex, expansion wave and oblique shock wave is distinctly captured in the turbulent calculation.

ACKNOWLEDGEMENTS

Support by the National Science Council of the Republic of China under Contract NSC 91-2212-E-150-026 is gratefully acknowledged.

REFERENCES

1. McDonald H. Turbulent shear layer reattachment with special emphasis on the base pressure problem. *The Aeronautical Quarterly* 1964; **15**:247–279.
2. Rom J. Analysis of the near wake pressure in supersonic flow using the momentum integral method. *Journal of Spacecraft and Rockets* 1966; **3**(10):1504–1509.
3. Samimy M, Petrie HL, Addy AL. A study of compressible turbulent free shear layers using laser doppler velocimetry. *AIAA Paper No.* 85-0177, 1985.
4. Abu-Hijleh B, Samimy M. An experimental study of a reattaching supersonic shear layer. *AIAA Paper No.* 89-1801, 1989.
5. Arai T, Sugiyama H, Homareda M, Uno N. Turbulence characteristics of supersonic boundary layer past a backward facing step. *AIAA Paper No.* 95-6126, 1995.
6. Hartfield RJ, Hollo SD, McDaniel JC. Planar measurement technique for compressible flows using laser induced iodine fluorescence. *AIAA Journal* 1993; **31**(3):483–490.
7. Loth E, Kailasanath K, Lohner R. Supersonic flow over an axisymmetric backward-facing step. *Journal of Spacecraft and Rockets* 1992; **29**(3):352–359.
8. Yang SY. Adaptive analysis of the inviscid supersonic flow over a backward-facing step. *Journal of Propulsion and Power* 2001; **17**(4):938–940.
9. Kuruvila G, Anderson JD. A study on the effects of numerical dissipation on the calculations of supersonic separated flow. *AIAA Paper No.* 85-0301, 1985.
10. Lombard CK, Luh RCC, Nagaraj N, Bardina J, Venkatapathy E. Numerical simulation of backward step and jet exhaust flows. *AIAA Paper No.* 86-0432, 1986.
11. Yang AS, Hsieh WH, Kuo KK. Theoretical study of supersonic flow separation over a rearward facing step. *AIAA Paper No.* 91-2161, 1991.
12. Tucker PK, Shyy W. A numerical analysis of supersonic flow over an axisymmetric afterbody. *AIAA Paper No.* 93-2347, 1993.
13. Halupovich Y, Natan B, Rom J. Numerical solution of the turbulent supersonic flow over a backward facing step. *Fluid Dynamics Research* 1999; **24**:251–273.
14. Chen YS, Farmer RC. CFD analysis of baffle flame stabilization. *AIAA Paper No.* 91-1967, 1991.
15. Sheng C, Whitfield DL, Anderson WK. Multiblock approach for calculating incompressible fluid flows on unstructured grids. *AIAA Journal* 1999; **37**(2):169–176.
16. Mavriplis DJ. Viscous flow analysis using a parallel unstructured multigrid solver. *AIAA Journal* 2000; **38**(11):1243–1251.
17. Rausch RD, Batina JT, Yang HTY. Spatial adaptation of unstructured meshes for unsteady aerodynamic flow computations. *AIAA Journal* 1992; **30**(5):1243–1251.
18. Hwang CJ, Wu SJ. Global and local remeshing algorithms for compressible flows. *Journal of Computational Physics* 1992; **102**(1):98–113.

19. Webster BE, Shephard MS, Rusak Z, Flaherty JE. Automated adaptive time-discontinuous finite element method for unsteady compressible airfoil aerodynamics. *AIAA Journal* 1994; **32**(4):748–757.
20. Pirzadeh SZ. A solution-adaptive unstructured grid method by grid subdivision and local remeshing. *AIAA Journal* 2000; **37**(5):818–824.
21. Walsh PC, Zingg DW. Solution adaptation of unstructured grids for two-dimensional aerodynamic computations. *AIAA Journal* 2001; **39**(5):831–837.
22. Oh WS, Kim JS, Kwon OJ. Numerical simulation of two-dimensional blade–vortex interactions using unstructured adaptive meshes. *AIAA Journal* 2002; **40**(3):474–480.
23. Yang SY. Adaptive strategy of transonic flows over vibrating blades with interblade phase angles. *International Journal for Numerical Methods in Fluids* 2003; **42**(8):885–908.
24. Reddy KC, Jacock JL. A locally implicit scheme for the Euler equations. *AIAA Paper No.* 87-1144, 1987.
25. Hwang CJ, Liu JL. Inviscid and viscous solutions for airfoil/cascade flows using a locally implicit algorithm on adaptive meshes. *Journal of Turbomachinery* 1991; **113**(4):553–560.
26. Abe K, Kondoh T. A new turbulence model for predicting fluid flow and heat transfer in separating and reattaching flows—I. flowfield calculations. *International Journal of Heat and Mass Transfer* 1994; **37**(1): 139–151.
27. Nagano Y, Tagawa M. An improved k–ε model for boundary layer flows. *Journal of Fluids Engineering* 1990; **112**(2):33–39.
28. Jameson A, Schmidt W, Turkel E. Numerical solutions of the Euler equations by finite volume methods using Runge–Kutta time-stepping schemes. *AIAA Paper No.* 81-1259, 1981.
29. Mavriplis DJ. Accurate multigrid solution of the Euler equations on unstructured and adaptive Meshes. *AIAA Journal* 1990; **28**(2):213–221.
30. Nayani SN. A locally implicit scheme for Navier–Stokes equations. *Ph.D. Thesis*, The University of Tennessee, Knoxville, Tennessee, 1988.
31. Hwang CJ, Fang JM. Solution-adaptive approach for unsteady flow calculations on quadrilateral–triangular meshes. *AIAA Journal* 1996; **34**(4):851–853.
32. Thibert JJ, Granjacques M, Ohman LH. Experimental data base for computer program assessment, *NACA 0012 airfoil AGARD advisory Report No. 138*. 1979; A1-9.

